Nuclear charge radii of $^{46-62}$Cr isotopes and reaction cross sections for p-Cr

M. Hemalatha*
Department of Physics, University of Mumbai, Mumbai 400098, India

(Received 16 June 2022; revised 24 August 2022; accepted 1 November 2022; published 17 November 2022)

The nuclear charge radii and density distributions for $^{46-62}$Cr have been calculated in the frameworks of both relativistic and nonrelativistic self-consistent mean-field models. The relativistic Hartree-Bogoliubov model with density-dependent meson-exchange functional DD-ME2 and the nonrelativistic Hartree-Fock-Bogoliubov model with the Gogny D1S interaction, hereafter referred to as DIRHB and HFB, respectively, are used to compute ground-state properties of even $^{46-62}$Cr isotopes. Both calculations for the root-mean-squared charge radii reveal the characteristic kink at the $N = 28$ shell closure in accordance with the corresponding experimental radii. The point proton and neutron density distributions calculated from both DIRHB and HFB are used to obtain the optical potentials for p-Cr at an incident proton energy of 65 MeV. The elastic scattering differential and total reaction cross sections, computed from the semimicroscopic proton optical potentials, have been derived by folding each of the target matter densities with the Jeukenne-Lejeune-Mahaux-Bruyeŕes (JLMB) energy- and density-dependent internucleon interaction. The calculated elastic scattering differential cross sections for stable even isotopes, ^{50,52,54}Cr, using the respective DIRHB and HFB densities in the folding model reproduce the corresponding cross-section data well. The correlation between root-mean-squared charge radii and nuclear reaction observables obtained from the DIRHB and HFB calculations have been used in the folding model approach to predict the reaction cross sections for p-$^{46-62}$Cr at an incident proton energy of 65 MeV.

DOI: 10.1103/PhysRevC.106.054607

I. INTRODUCTION

An understanding of the evolution of charge radii and reaction cross sections with increasing neutron number gives insight into the structure and reactions of nuclei that span neutron-deficient to neutron-rich regions of the nuclear landscape [1–5]. The continuous progress in the production of a wide variety of radioactive ion beams from accelerator facilities around the world, coupled with the advancement in laser spectroscopic methods, are contributing to the investigations of various nuclear properties such as the binding energy and charge radius [6–9]. The region around the shell closures $N = 20$ and $N = 28$ have recently attracted attention owing to the manifestation of a variety of structures from spherical nature to collective behavior typical of deformed open-shell nuclei. Measurements and theoretical investigations of charge radii for stable and unstable nuclei have been carried out to determine the changing shell effects in the calcium region [10–25]. The measured root-mean-squared (rms) charge radii display various nuclear structure effects, including kinks in isotopic chains at well-established nuclear shell gaps. The rms charge radii have been measured for stable isotopes with $Z = 18$–26, while in the case of unstable isotopes, they have been determined only for three isotopic chains, $Z = 18$, 19, and 20. Laser spectroscopy measurements have been carried out for Ar [11], K [12–14], Ca [15,16], Sc [17], Ti [18], Cr [10], Mn [19,20], and Fe [21]. Although theoretical models predict certain structural changes in this region, the charge radii for many nuclei have yet to be measured.

It is well known that there is a distinct correlation between nuclear radii and the reaction cross sections. An example of such a correlation is the large increase in the measured interaction cross section between ^{9}Li and ^{11}Li and the large matter radius deduced thereof using a Glauber-type calculation [1]. In pioneering work on this aspect, the rms proton radii were related to the total charge-changing cross sections in light nuclei such as isotopes of Na ranging from proton to neutron drip lines, using the Glauber model [2,3]. Following this, nuclear charge radii in isotopic chains were connected to the total reaction cross section using the folding optical model calculations for Zr [4] and Ti [5] isotopic chains. The linkage between the nuclear structure and reaction observables can be done using the folding model framework through elastic scattering. When the nuclear structure information is obtained from well-established models, whether relativistic or nonrelativistic, the cross sections are well reproduced for nucleon-nucleus systems.

The Cr isotopic chain, with 24 protons, lies exactly in the middle of the two shell closures $N = 20$ and $N = 28$ and is therefore interesting to study. The relationship between charge radii and the reaction cross sections in the Cr isotopic chain is studied for p-Cr scattering using both relativistic and nonrelativistic structure models. In the present work, self-consistent mean-field models are used to generate ground-state properties such as nuclear binding energies, radii, and densities of even Cr isotopes ($A = 46$–62). The calculated nuclear

*mhemalatha.tandel@physics.mu.ac.in; mhemalatha.tandel@gmail.com

properties from the relativistic Hartree-Bogoliubov (RHB) model with the density-dependent meson-exchange (DD-ME2) relativistic energy density functional (EDF) [26,27] are compared with those from the nonrelativistic Hartree-Fock-Bogoliubov (HFB) model with the Gogny D1S interaction [28–30]. Each of these target matter density distributions is folded with the Jeukenne-Lejeune-Mahaux-Bruyeŕes (JLMB) interaction [31,32] that yields the respective optical model potentials. The optical model potentials are used to calculate the elastic scattering differential and total reaction cross sections for scattering of 65-MeV protons from even $^{46-62}$Cr isotopes.

The paper is organized as follows: the description of relativistic and nonrelativistic mean-field models is given in Sec. II. The results of the calculation of the ground-state properties using both the mean-field models for even isotopes of Cr are presented in Sec. III. Section IV gives details of the folding optical model using the JLMB nucleon-nucleon interaction. The results and discussions of the calculation of folded potentials as well as cross sections for elastic scattering of 65 MeV protons from even Cr isotopes are presented in Secs. V and VI.

II. SELF-CONSISTENT MEAN-FIELD (SCMF) MODELS

Nuclear density functional theory (DFT) is a powerful technique that facilitates the description of the ground-state energy of a nuclear system as a functional of the ground-state density alone. The basic execution has been in the form of a self-consistent mean-field model in which an EDF is constructed as a functional of the one-body nucleon density matrices. The EDFs are phenomenological and are determined by adjusting the model parameters to reproduce the properties of nuclear matter as well as the bulk properties of selected spherical and stable nuclei. Several HFB models based on nonrelativistic DFT have been developed [28,33]. Over several decades, both nonrelativistic and relativistic DFTs have enabled considerable progress in achieving the goal of predicting the structure properties with a high degree of confidence for nuclei across the periodic table, including those which are near drip lines. The nonrelativistic [34] and relativistic [35–38] DFT in nuclear physics have been extensively reviewed. One of the successes of the covariant (relativistic) DFT (CDFT), in contrast to nonrelativistic DFT, is the reproduction of the kinks in the systematics of charge radii for neutron shell closure for several isotopic chains, as discussed in a recent review [22]. An important aspect of the CDFT is the provision of the spin degree of freedom, unlike in nonrelativistic DFT where additional parameters are required to account for the spin-orbit interactions. The CDFT has been able to provide a good description of not only the ground-state properties but also the excitation properties of a variety of nuclei [39–41].

The formulation and development of the RHB model, which represents a relativistic extension of the conventional HFB framework, has been an important step for studying nuclei lying away from the line of stability. The description of existing nuclear structure data and the prediction of properties by relativistic mean-field models are comparable to, and recently even better than, nonrelativistic mean-field models [26,27,36,37]. Some examples of such theories are the RHB models with density-dependent meson-exchange (DD-ME2) relativistic (covariant) energy density functionals [26,27] and the nonrelativistic HFB theory with the Gogny D1S interaction [28–30]. The analysis of several nuclear structure properties has also been carried out through various other approaches using relativistic [4,5,42–44] and nonrelativistic mean-field models [34,45,46].

The continuum and pairing correlations play a critical role in the study of nuclei near drip lines. The relativistic continuum Hartree-Bogoliubov (RCHB) theory [47,48] has been able to provide a unified and self-consistent treatment of pairing correlations and mean-field potentials in the presence of the continuum. The RCHB theory was able to successfully provide the first microscopic self-consistent description of the halo in ^{11}Li and predicted the giant halos in light and medium-heavy nuclei [38]. By taking the deformation into account, a deformed RCHB theory was developed [49,50]. The application of deformed RHB theory in the continuum (DRHBc) based on one of the most successful relativistic density functionals, PC-PK1 [51] for even-even nuclei was successfully done for the case of Nd isotopes [52]. Recently, the predictive power of DRHBc theory for nuclei in the superheavy region, and also that of possible stability beyond the neutron drip line, was investigated [53].

The RHB model with DD-ME2 functional and HFB model with Gogny D1S interaction are compared in the present work.

A. RHB model with DD-ME2 functional

The Dirac-RHB (DIRHB) approach with the explicit DD-ME2 model [26,27] provides a precise global description of a variety of nuclear structure phenomena of even-even deformed nuclei. In the RHB framework, an effective Lagrangian is routinely used to express the Dirac spinor nucleons interacting through various exchange mesons. The account of single-particle and bulk properties of nuclei is provided by a minimal set of meson fields arising from the σ, ω, and ρ mesons as well as the electrostatic potential. The model provides a treatment of the SCMF ($\hat{h}_D$) and pairing field ($\hat{\Delta}$) by means of two average potentials. $\hat{h}_D$ describes the long-range particle-hole (ph) correlations, while the particle-particle (pp) correlations are taken into account by ($\hat{\Delta}$). The RHB equations are given by

$$\begin{pmatrix} \hat{h}_D - m - \lambda & \hat{\Delta} \\ -\hat{\Delta}^* & -\hat{h}_D^* + m + \lambda \end{pmatrix} \begin{pmatrix} U_k \\ V_k \end{pmatrix} = E_k \begin{pmatrix} U_k \\ V_k \end{pmatrix},$$

where $\hat{h}_D$, m, and λ are the single-nucleon Dirac Hamiltonian, nucleon mass, and Fermi energy, respectively. The coefficients U_k and V_k are the quasiparticle Dirac spinors, while E_k is the quasiparticle energy. The $\hat{\Delta}$ is obtained from the pairing tensor and two-body nuclear potential $V_{\rm pp}$ in the pp channel. Since there is no empirical evidence for relativistic effects in $\hat{\Delta}$, a hybrid RHB model with a nonrelativistic pairing interaction is generally used. Therefore, $V_{\rm pp}$ is described by a separable pairing force having a finite range [54].

A combination of the configurational and coordinate space representations by Vautherin [33] is used in the RHB model for efficient execution. This method can be implemented for spherical, axially deformed, and triaxial nuclei. The vector and scalar densities obtained are used to compute the required potentials. The RHB equations are to be solved in a self-consistent way, with potentials obtained in the mean-field approximation from solutions of the Klein-Gordon equations that describe the meson fields. Explicit calculations require parameters appearing in the Lagrangian and $V_{\rm pp}$ as input. The RHB calculations yield single-particle energies, nucleon spinors, fields, occupancies, total binding energy, deformations, rms radii, currents, and densities. The RHB equations are solved iteratively in an axially deformed harmonic oscillator basis. The number of oscillator shells taken into account in the expansion was $N_F^{\rm max} = 12$ fermionic shells for the Dirac spinors and $N_B^{\rm max} = 20$ bosonic shells for the meson fields. The deformation parameter (β_2) for the harmonic oscillator basis and for the initial Woods-Saxon potential was set to be zero. It should be noted that pairing correlations are treated in the BCS constant-gap approximation with empirical pair gaps (five-point formula) [55], while the EDF parameters are adjusted for DD-ME2.

B. Nonrelativistic HFB model with Gogny D1S interaction

The microscopic HFB method using the Gogny D1S effective nucleon-nucleon interaction [28,30] has been successfully used for nuclear structure studies for a variety of nuclei. A detailed description of the HFB theory is presented in several references [29,56–58]. Delaroche *et al.* [30] have carried out a large-scale systematic study of the structure at low energy with normal deformation using the constrained-HFB theory along with a mapping to the five-dimensional collective Hamiltonian, employing the Gogny D1S interaction in the nuclear Hamiltonian [28,56]. The constrained axially symmetric HFB-D1S calculations for isotopes of C ($Z = 6$) to Ds ($Z = 110$) for even-even nuclei from proton to neutron drip lines have been performed with a common set of parameters for all properties studied. Compilations of calculations of the global ground- and excited-state properties of thousands of nuclides are available online [59]. Some global properties presented include the positions of the drip lines, ground-state radii, intrinsic quadrupole shape parameters, and binding energies. The radial matter densities required to perform optical-model calculations have also been made available. The neutron and proton densities are tabulated in the radius grid in steps of 0.1 fm up to a maximum value of 15 fm.

In the present work, the RHB calculation using the DD-ME2 interaction is referred to as DIRHB, while the HFB calculation with the Gogny D1S interaction is denoted by just HFB.

III. CALCULATED GROUND-STATE PROPERTIES FOR Cr ISOTOPES

A. Charge radii

The reliability of the calculations depends on the consistent understanding of fundamental properties of the ground state, such as binding energies (obtained from the nuclear masses) and rms radii (determination of the nuclear size and shape). The study of nuclear properties as a function of the number of neutrons gives a deeper understanding of the variation of properties with isospin, and thereby important nuclear structure information can be obtained.

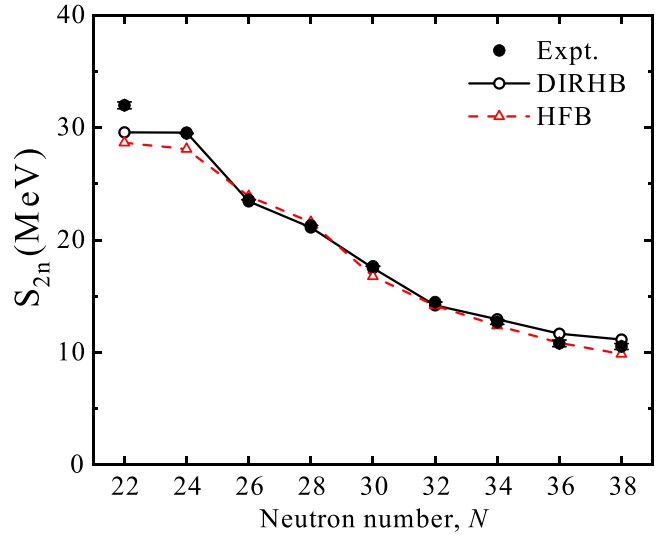

FIG. 1. The calculated two-neutron separation energies (S_{2n}) using the DIRHB and HFB models. The corresponding experimental values [60] are also shown.

The binding energy (E_b) and two-neutron separation energy (S_{2n}) were obtained for the isotopes $^{46-62}$Cr from the DIRHB as well as the HFB calculations and compared with available data [60]. The calculated E_b and S_{2n} were further compared with those from spherical RCHB [61] and deformed DRHBc [25] and are found to agree well. The agreement of the calculated E_b for the Cr isotopic chain is found to be within 1% of the corresponding experimental values [42]. The S_{2n} calculated from the DIRHB and HFB are displayed in Fig. 1. Both the DIRHB and HFB calculations show a characteristic decrease in S_{2n} with an increase in neutron number, and the systematics are in agreement with those from experiment [60] as well as those listed using the DRHBc calculation.

The difference between the rms charge radii of the even-even isotopes of Cr ($N = 22$–38) and that of the closed-shell nucleus, ^{52}Cr ($N = 28$) is represented by the expression, $\delta\langle r_c^2\rangle^{N,28} = \langle r_c^2\rangle^{N} - \langle r_c^2\rangle^{28}$. It is well known that the $\delta\langle r_c^2\rangle^{N,28}$ is precisely measured through laser spectroscopy measurements and serves as a test for discriminating between theoretical models. The $\delta\langle r_c^2\rangle^{N,28}$ calculated using both the DIRHB and HFB are shown in Fig. 2, for even isotopes of Cr. The measured $\delta\langle r_c^2\rangle^{N,28}$ are available in the literature for ^{50,52,54}Cr [10]. As seen in Fig. 2 in the case of ^{50}Cr ($N = 26$), both the DIRHB and HFB values of $\delta\langle r_c^2\rangle^{N,28}$ agree with each other; however, they are slightly higher than the experimental value. The HFB value of $\delta\langle r_c^2\rangle^{N,28}$ for $N = 30$ agrees quite well with the corresponding datum, while the DIRHB value is slightly higher. The experimental $\delta\langle r_c^2\rangle^{N,28}$ values for ^{50,54}Cr are overestimated by the DIRHB calculations. This indicates that there could be effects beyond the mean field that affect the ground-state properties of the nuclei with $N = 26, 30$ having prolate

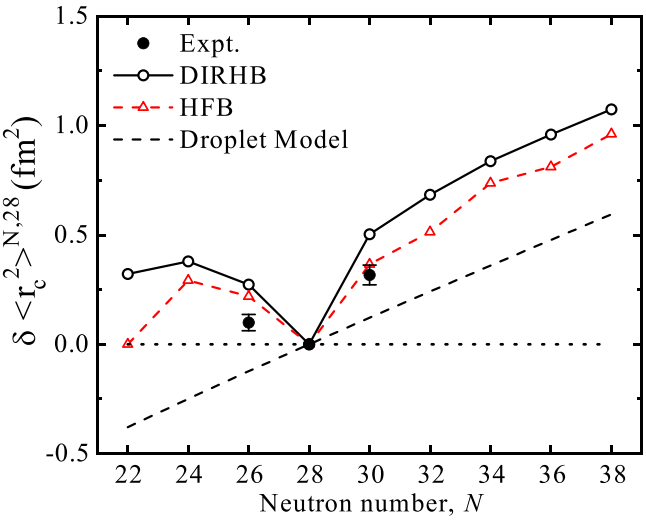

FIG. 2. The difference ($\delta\langle r_c^2\rangle^{N,28}$) between the rms charge radii of even-even isotopes of Cr and that of the closed-shell nucleus ^{52}Cr ($N = 28$) calculated using the DIRHB and HFB models. The corresponding experimental values [10] (where available) are shown for comparison. The dashed line indicates $\delta\langle r_c^2\rangle^{N,28}$ values obtained using the droplet model [65].

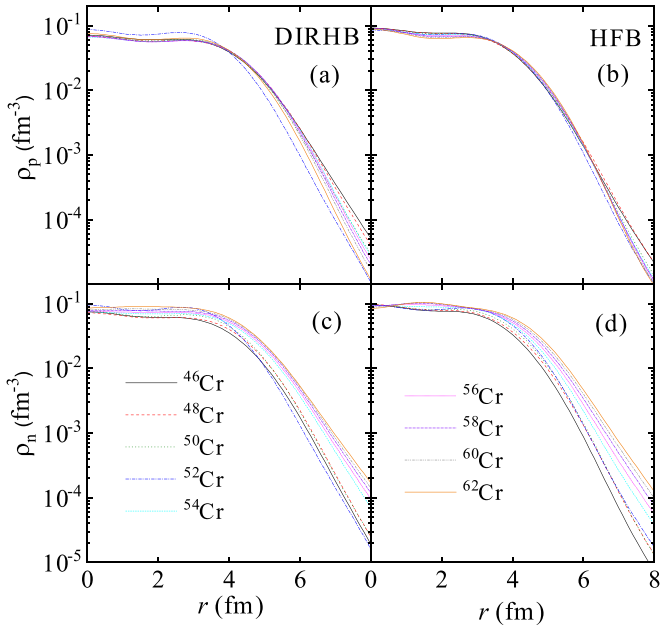

FIG. 3. The calculated DIRHB and HFB ($L = 0$ component) proton [(a) and (b)] and neutron [(c) and (d)] densities, normalized to Z and N, respectively, for even Cr isotopes.

deformation [22]. The variation in nuclear charge radii can be explained by studying quadrupole deformation [62]. Both the DIRHB and HFB calculations show maximum $\delta\langle r_c^2\rangle^{N,28}$ values for mid-neutron-shell nucleus ^{48}Cr ($N = 24$). The half-filled shells are deformed and, consequently, are associated with large quadrupole moments and charge radii. It is interesting to note that similar behavior of $\delta\langle r_c^2\rangle^{N,28}$ is seen in the Ti and Fe isotopic chains [5,63,64].

A comparison of the DIRHB and the HFB values of $\delta\langle r_c^2\rangle^{N,28}$ with the spherical droplet model [65] is also presented in Fig. 2. It is seen that the droplet model shows consistently lower values for radii as compared to the DIRHB and HFB ones, and shows no kink. In the neutron-rich isotopes of Cr, a steady increase in the DIRHB and HFB radii with the addition of neutrons is seen, beyond $N = 30$. There is a change in the slope in $\delta\langle r_c^2\rangle^{N,28}$ at $N = 30$, while a different behavior is seen in the neutron-deficient region for both the calculations and experiment. Both calculations for $\delta\langle r_c^2\rangle^{N,28}$ reproduce the experimental anomalous behavior (i.e., nuclei with fewer neutrons compared to $N = 28$ show increased radii, while a decrease is expected from the droplet model). It is also seen that, as neutrons are removed from ^{52}Cr, the $\delta\langle r_c^2\rangle^{N,28}$ increases followed by a decrease towards $N = 22$. The $\delta\langle r_c^2\rangle^{N,28}$ for $^{46-62}$Cr, calculated from DIRHB and HFB, agree well with those tabulated for DRHBc [25]. The measured values of nuclear charge radii through the isotope shift method using laser spectroscopy for radioactive Cr isotopes is required to substantiate the predictions and understand their behavior.

B. Point proton and neutron density distributions

Once the calculations of ground-state properties are found to be in agreement with the experimental data, the point proton and neutron density distributions that are required for the calculation of the optical model potential can be carried out. For axially deformed target nuclei, the nuclear density distributions are expressed in terms of a multipole expansion with Legendre polynomials [33,66]. The multipole decomposition of the density distribution can be written in terms of multipole components L, and normalized to the numbers of protons and neutrons, respectively. A component with a higher L has a smaller contribution to the density distribution, and with increasing deformation the contribution of higher-order components becomes larger. For the even isotopes, $^{46-62}$Cr, the $L = 0$ components of the DIRHB and HFB point proton (ρ_p) and neutron (ρ_n) density distributions are considered and are normalized to respective proton and neutron numbers. They are shown in Fig. 3 and their features are discussed. Both ρ_p and ρ_n from the DIRHB and HFB calculations are quite similar in the nuclear interior for all the isotopes shown. There is less dispersion of ρ_p from the HFB calculations in the surface region compared to those from the DIRHB ones. As expected, ρ_p from DIRHB and HFB has the lowest spread for isotopes with $N = 28$, while it is more extended and similar in nature to isotopes with $N = 22, 24$. The ρ_p distribution for $N = 26$, 30–38 closely resemble one another, with $N = 38$ having less spread in the surface region. In the cases of $N = 22$–28, the ρ_n distribution in the surface region extends over smaller distances as compared to the $N = 30$–38 isotopes. Figure 3 also indicates that ^{46}Cr has the least spread in ρ_n for the HFB calculation.

The point proton and neutron density distributions from the DIRHB and HFB calculations for the even isotopes of Cr are used in the folding model analysis, which is discussed in the next section.

IV. FOLDING OPTICAL MODEL USING JLMB INTERACTION

The folding model has been successful in establishing a direct connection between the nuclear structure and the reaction observables through elastic scattering. The behavior of the nuclear density distributions and, therefore, the nuclear charge radii of the isotopes are reflected in the reaction cross sections. The connection can be used to predict the reaction cross sections, especially for radioactive nuclei, where data are scarce. Making a successful prediction of the reaction cross sections relies on the radial matter densities being derived from well-tested structure models, either relativistic or nonrelativistic [67,68]. Similar considerations are applicable for the microscopic, spherical nucleon-nucleus optical model potentials based on different approximations or effective forces [32,69–74]. Both microscopic [75,76] and phenomenological [77] optical models have been successful in describing nucleon-nucleus scattering. However, the microscopic calculation of potentials is essential for understanding the subtle changes in cross sections of nuclei as a function of neutron number. The nucleon-nucleus optical model potential (OMP) is constructed, in the single-folding model approach, by integrating a complex energy- and density-dependent nucleon-nucleon effective interaction with the nuclear density distributions describing the target nucleus.

In the present work, an extended version [32] of the original Jeukenne, Lejeune, and Mahaux (JLM) potential [31] relying on the Brückner-Hartree-Fock approximation was used that provides a good overall description of nucleon scattering and reaction observables. The JLM interaction established for nuclear matter was made suitable for finite nuclei, by applying a local density approximation, and is further extended to deformed nuclei. For reproduction of the experimental scattering and reaction observables, a suitable spin-orbit potential, in addition to an appropriate central potential, is required. The JLM model [31] provides only the central potential, and therefore a phenomenological prescription [78] that is applicable for higher energies was used to calculate the deformed complex spin-orbit potential in the full Thomas form. The resulting potential, referred to as JLM-Bruyéres (JLMB) [32], is complex, spin-independent, energy- and density-dependent, and suitable for energies from 1 to 200 MeV. The input point proton and neutron densities of the target used in the folding model were calculated in the DIRHB and HFB frameworks as described in the previous section. Using the semimicroscopic approach, the folding OMPs are obtained for the elastic scattering of 65 MeV protons from even isotopes of Cr ($N = 22$–38). The JLMB potential that gives the real and imaginary parts of the central and spin-orbit OMPs is calculated. The folding of the JLM internucleon interaction with the calculated DIRHB and HFB densities, respectively, is carried out to calculate the differential elastic scattering and total reaction cross sections for the even isotopes of $^{46-62}$Cr.

The spherical JLMB optical model, used in the present study, treats the target nucleus as spherical. However, the observations indicate that all Cr isotopes, except ^{52}Cr, are deformed and collectivity sets in for open-shell nuclei, $^{46-50,54-62}$Cr [79,80]. The coupled-channels method [81] can be used to describe simultaneously the elastic scattering channel and the low-lying states that, due to their collective nature, are strongly excited in inelastic scattering. It is important to note that the coupled-channel effects play an important role at lower energies and not at the proton energy of 65 MeV, and, therefore, are not considered in the present calculations.

V. CALCULATED POTENTIALS FOR PROTON ELASTIC SCATTERING FROM Cr ISOTOPES

Folding of the JLMB nucleon-nucleon interaction with each of the calculated DIRHB and HFB densities, for the elastic scattering of 65 MeV protons from even isotopes of Cr was performed using the code MOM (Microscopic Optical Model) [32]. The folding model gives both the real [$V(r)$] and imaginary [$W(r)$] parts of the central as well as the real [$V_{so}(r)$] and imaginary [$W_{so}(r)$] parts of the spin-orbit optical model potentials as a function of radial distance (r). The semimicroscopic OMP, $U_{\rm JLMB}(r, E)$, can be expressed as

$$U_{\rm JLMB}(r, E) = \lambda_V V(r, E) + i\lambda_W W(r, E) + \frac{\hbar^2}{2m^2c^2}(\bar{l}\cdot\bar{\sigma})\left[\lambda_{V\,so}V_{so}(r, E) + i\lambda_{W\,so}W_{so}(r, E)\right],$$

where λ_V, λ_W, $\lambda_{V\,so}$, and $\lambda_{W\,so}$ are the energy (E) dependent renormalization factors for the real and imaginary central as well as spin-orbit parts of the OMP, respectively. The λ's provide the overall renormalization of the calculated OMP that is essential for obtaining a good agreement with the elastic scattering differential cross-section data and takes into account any deficiency in the potential.

An available version of the code ECIS06 [82] was used for the calculation of elastic scattering and total reaction cross sections. The code performs a search on λ's that provides a minimum in χ^2 by fitting the differential cross-section data for stable isotopes. At the incident proton energy of 65 MeV, both the central and spin-orbit interactions are important for calculating the cross sections for proton scattering off Cr isotopes. Since the focus here is the prediction of cross sections, it is important to use a minimum number of parameters (λ) in the process. By conducting a search on all the λ's, it was found that $\lambda_{W\,so}$ was small, and, since it did not have much influence on the calculated cross sections, it was neglected. In a previous calculation for the neighboring isotopic chain of Ti [5], satisfactory results for proton scattering at an incident energy of 65 MeV were obtained. For the sake of consistency, in the comparison of cross sections in the $N = 28$ region, the value of $\lambda_{V\,so} = 88$ for the Cr isotopic chain was fixed. There are now only two parameters, λ_V and λ_W, in the calculation. With $\lambda_{V\,so}$ fixed at 88, a search was carried out on λ_V and λ_W for χ^2 minimization and a good agreement of the calculated differential cross section with the data for stable isotopes, ^{50,52,54}Cr, was obtained. The values are referred to as the best-fit values (plotted in Fig. 5). The resulting values λ_V and λ_W were slightly different for folding-model calculations using DIRHB compared to those using HFB densities.

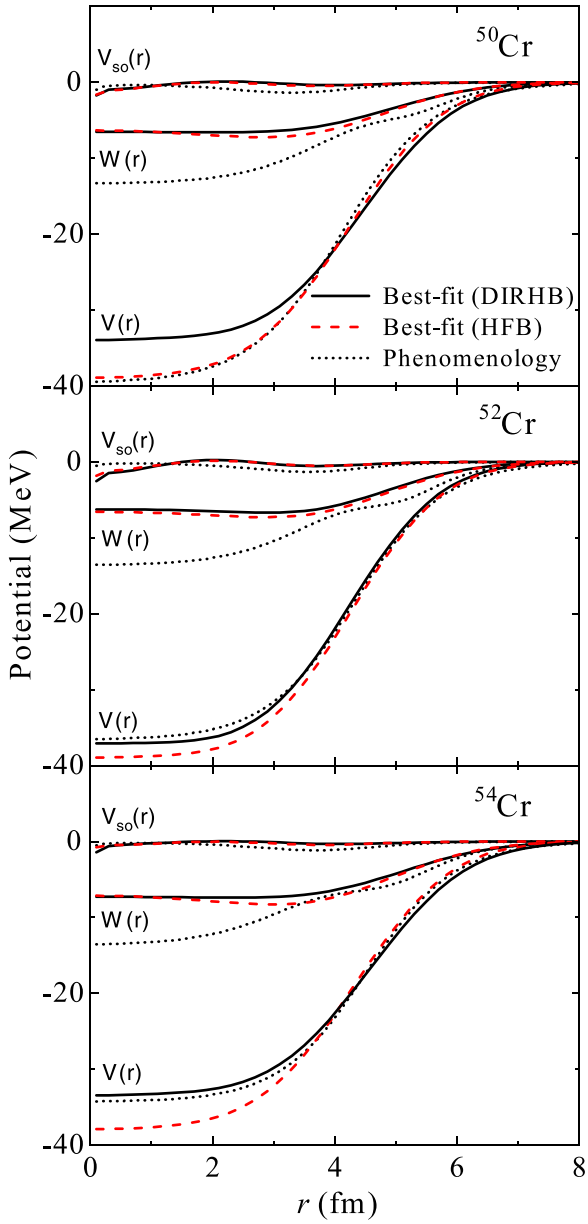

FIG. 4. The renormalized real central, imaginary central, and real spin-orbit parts of the folded potential using best-fit values of λ_V and λ_W for the scattering of protons from stable even-Cr isotopes. The corresponding phenomenological [83] Woods-Saxon (WS) potentials are also shown.

The best-fit values are used to calculate the renormalized $V(r)$, $W(r)$, and $V_{so}(r)$ as shown in Fig. 4 for stable isotopes. The potentials determined from the above semimicroscopic calculations are compared with those of the corresponding phenomenological Woods-Saxon (WS) ones [83], and those as a function of radial distance (r) are shown in Fig. 4. It is seen from Fig. 4 that there is agreement of $V(r)$, $W(r)$, and $V_{so}(r)$ with the corresponding WS parts of the potentials in the surface region. The WS potential is deeper and different compared to both $W(r)^{\rm DIRHB}$ and $W(r)^{\rm HFB}$. The $V(r)^{\rm DIRHB}$ and $V(r)^{\rm HFB}$ for ^{50}Cr are deeper compared to the WS potential,

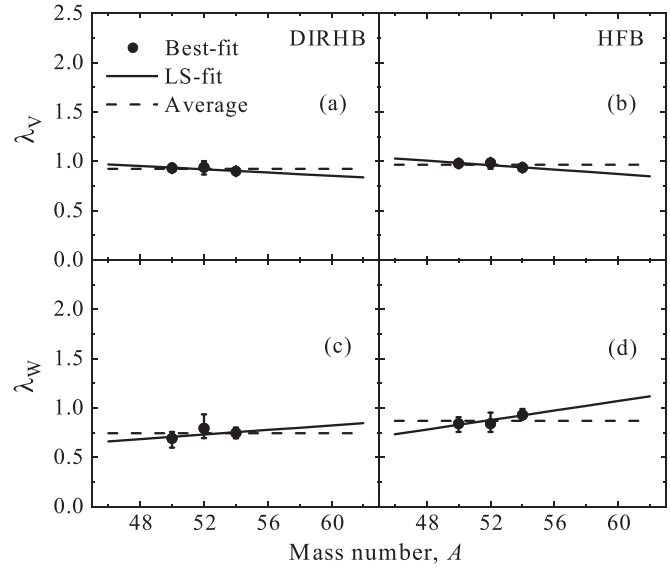

FIG. 5. Top panels, (a) and (b): Renormalization constants (λ_V) for real parts of the central potential. Bottom panels, (c) and (d): Renormalization constants (λ_W) for imaginary parts of the central potential. The results are obtained for proton scattering from even-Cr isotopes using the DIRHB and HFB densities as well as JLMB interaction in the folding model. The λ_V and λ_W values from a least-squares (LS) fit and average values are shown by solid and dashed lines, respectively. The corresponding best-fit values for stable isotopes are shown by solid circles.

while for ^{52,54}Cr the potential is deeper for HFB compared to DIRHB and WS in the interior region.

A least-squares (LS) fit to the best-fit values of λ_V and λ_W was carried out to obtain λ_V and λ_W values for the radioactive Cr isotopes. The renormalization constants for real, λ_V [Figs. 5(a) and 5(b)], and imaginary, λ_W [Figs. 5(c) and 5(d)], central parts of the potential for proton scattering from even-Cr isotopes using the DIRHB and HFB densities as well as the JLMB interaction in the folding model, respectively, are shown in Fig. 5. Linear relations between λ_V and λ_W, respectively, with A for the Cr isotopic chain, are given by the equations

$$\text{DIRHB: } \lambda_V = -0.0082A + 1.347,\ \lambda_W = 0.0116A + 0.131;$$
$$\text{HFB: } \lambda_V = -0.0112A + 1.547,\ \lambda_W = 0.2410A - 0.376,$$

As expected, λ_V have values approaching unity for both calculations. The slope of λ_V and λ_W obtained in calculations given in Fig. 5 for $A = 22$–38 is small. The average values of λ_V and λ_W are 0.9255 and 0.7443, respectively, for the calculation using DIRHB densities, while they are 0.9668 and 0.8707, respectively, for the calculation using the HFB densities. They are plotted in Fig. 5. The errors in λ_V and λ_W are obtained by changing λ_V and λ_W, respectively, to obtain a variation twice χ^2 from the corresponding best-fit values.

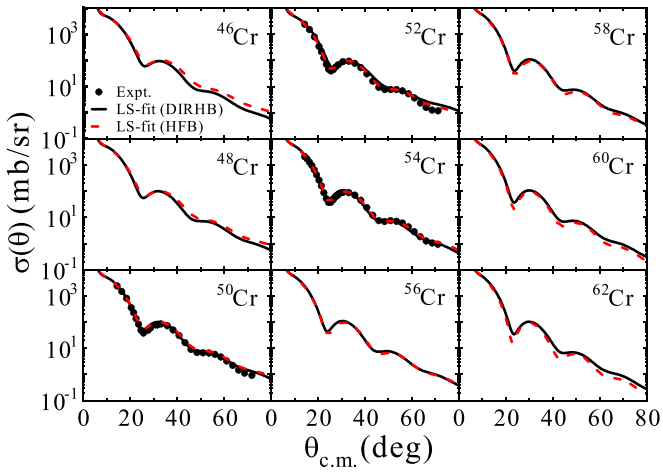

FIG. 6. The elastic scattering differential cross section $[\sigma(\theta)]$ as a function of center of mass (c.m.) angle, calculated using the DIRHB and HFB densities as well as the JLMB interaction in the folding model for the scattering of the 65 MeV protons from even Cr isotopes. The corresponding experimental values [83] available for stable Cr isotopes are shown. The $\sigma(\theta)$ are calculated using least-squares (LS) fit values of λ_V and λ_W.

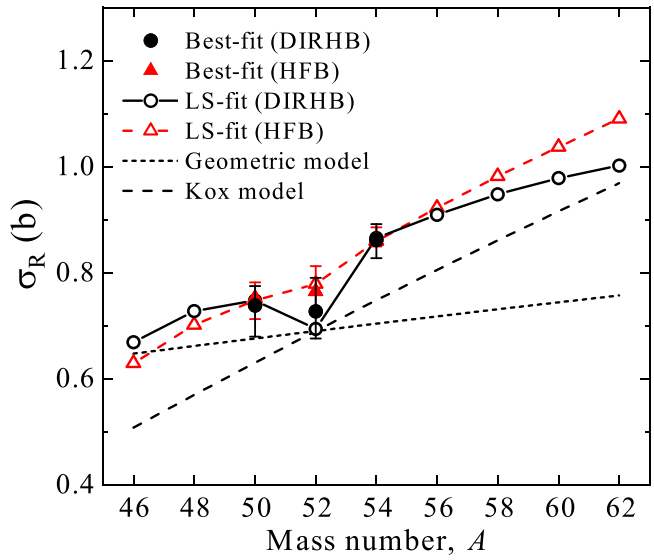

FIG. 7. The total reaction cross section (σ_R) calculated using the DIRHB and HFB densities as well as the JLMB interaction in the folding model for the scattering of 65 MeV protons from even-Cr isotopes. The σ_R are calculated using the best-fit and least-squares (LS) fit values of λ_V and λ_W. The σ_R from geometric and Kox [84,85] models are indicated by dotted and dashed lines, respectively.

VI. SCATTERING AND REACTION CROSS SECTIONS FOR Cr ISOTOPES

Using the renormalized OMP constructed by folding the JLMB interaction and two different types of density distributions, namely, DIRHB and HFB, as described in the previous section, the elastic scattering differential and total reaction cross sections are calculated using the code ECIS06 [82]. This semimicroscopic approach is used in the analysis of proton elastic scattering on stable and radioactive even isotopes of Cr ($A = 46$–62). The cross sections are calculated using the best-fit, LS-fit, and average values of λ_V and λ_W, keeping $\lambda_{Vso} = 88$ fixed.

A. Elastic scattering differential cross section

The elastic scattering differential cross sections $[\sigma(\theta)]$ calculated using the least-squares fit values of λ_V and λ_W for the scattering of 65 MeV protons from Cr isotopes, employing the DIRHB and HFB densities as well as JLMB interaction in the folding model, are given in Fig. 6. The corresponding experimental [83] differential cross-section values available for stable isotopes are also plotted in the same figure. It is seen that the calculated values using the DIRHB and HFB densities in the folding model for the stable ^{50,52,54}Cr isotopes are in good agreement with the corresponding data [83]. Overall, the features of the angular distribution are quite similar for all Cr isotopes under consideration. However, the first minimum becomes slightly deeper with an increase in neutron number. It may be noted that there are no differential cross-section data available for proton scattering from unstable Cr isotopes at 65 MeV. The predictions of elastic scattering differential cross sections for neutron-deficient ^{46,48}Cr and neutron-rich ^{56,58,60,62}Cr, are made using the semimicroscopic approach.

B. Total reaction cross section

Total reaction cross sections (σ_R) calculated using DIRHB and HFB densities, as well as the JLMB interaction in the folding model, using the least-squares fit values for even-Cr isotopes are shown in Fig. 7. The calculated σ_R obtained for stable ^{50,52,54}Cr isotopes using the best-fit values of λ_V and λ_W are also shown in the same figure. The errors in the calculation of σ_R have been included to note the sensitivity with respect to the change in renormalization constants, λ_V and λ_W. The errors in the best-fit values of σ_R, as shown in Fig. 7, for the stable isotopes are deduced by the same method applied in the cases of λ_V and λ_W. To understand and compare the behavior of the calculated σ_R in the present work with basic representations, σ_R from geometric (σ_R^g) and Kox [84,85] (σ_R^K) models, are also plotted in Fig. 7. The Kox model is based on the simple concept of strong absorption, while the geometric cross section is calculated using the simple relation $\sigma_R^g = \pi\, r_0^2\, (A_p^{1/3} + A_{Cr}^{1/3})^2$. The cross sections obtained from the geometric and Kox models were normalized to the extrapolated experimental cross section for ^{52}Cr ($N = 28$), i.e., 0.69 b, as explained below. The σ_R^g and σ_R^K both show a smooth increase with a change in neutron number; however, their slopes are different, with the Kox model exhibiting a larger slope. As expected, calculations for both σ_R^g and σ_R^K cannot reproduce the kink at the $N = 28$ shell gap, which is a typical feature of the variation of σ_R with N.

Although an experimental value of σ_R at a proton energy of 65 MeV is not available, a value of $\sigma_R = 0.708 \pm 0.190$ b [86] has been measured for scattering of 60.8 MeV proton beam from a ^{52}Cr ($N = 28$) target. Therefore, a simple extrapolation using the trend inferred from available σ_R data for the scattering of protons, at various incident energies, from neighboring

even-even target nuclei [87] was carried out to estimate σ_R for ^{52}Cr at 65 MeV. The $\sigma_R^{\mathrm{DIRHB}}$ determined for the scattering of 65 MeV protons from a ^{52}Cr ($N = 28$) target is about 0.69 b, which is in agreement with the above extrapolated value. The σ_R^{HFB} obtained in the case of ^{52}Cr is much higher than that of $\sigma_R^{\mathrm{DIRHB}}$. There is a monotomic increase in σ_R^{HFB} as a function of neutron number with no kink at the $N = 28$ shell closure. However, a kink at $N = 28$ is clearly evident in the variation of $\sigma_R^{\mathrm{DIRHB}}$ with neutron number similar to that seen in the $\delta\langle r_c^2\rangle^2$ systematics of Fig. 2. It would be interesting to study the correlation between σ_R and $\langle r_c^2\rangle^2$ for neighboring isotopic chains.

VII. CONCLUSION

Two different models, the relativistic Hartree-Bogoliubov (RHB) model with density-dependent meson-exchange (DD-ME2) relativistic energy density functional and the non-relativistic mean-field model based on the Hartree-Fock-Bogoliubov (HFB) theory with the Gogny D1S interaction, were used to calculate the nuclear ground-state properties for even isotopes $^{46-62}$Cr. The DIRHB and HFB calculations for the ground-state properties, such as root-mean-squared charge radii, successfully describe the kinks at the $N = 28$ shell closure observed in the corresponding data. The point proton and neutron density distributions calculated from the RHB and HFB models, respectively, are convoluted with the Jeukenne-Lejeune-Mahaux-Bruyeŕes (JLMB) internucleon interaction, to obtain the optical potential. Real and imaginary central as well as real spin-orbit potentials are used to compute the cross section for the scattering of 65 MeV protons from even $^{46-62}$Cr isotopes. The elastic scattering differential cross sections calculated from the folding model analysis using the DIRHB and HFB densities as well as the JLMB interaction agree well with the corresponding experimental values for stable even Cr isotopes. The prediction of σ_R for even $^{46-62}$Cr isotopes was presented using both the relativistic and nonrelativistic self-consistent mean-field models. The semimicroscopic folding model calculation using the DIRHB densities is able to reproduce the kink at $N = 28$ in the variation of the total reaction cross section, similar to that observed in the variation of the root-mean-squared charge radii for Cr isotopes. The calculation with nonrelativistic HFB densities shows a monotomic increase in reaction cross section and no kink is visible in the variation with neutron number for the Cr isotopic chain. Measurements of reaction cross sections in existing radioactive ion-beam accelerator facilities are expected to validate the predictions presented here for the scattering of 65 MeV protons from even-Cr isotopes.

ACKNOWLEDGMENTS

M.H. expresses grateful to Prof. T. Nikšić and Prof. D. Vretenar for guidance in the calculation of nuclear ground-state properties using DIRHB. The assistance of N. Maladkar is acknowledged. M.H. thanks Dr. S. Kailas and Prof. Y. K. Gambhir for a critical reading of the manuscript and useful comments. The support of the University Grants Commission, India, under the Faculty Recharge Program and Department of Science and Technology (DST) Science and Engineering Research Board (SERB), Government of India, File No. CRG/2021/008396, is acknowledged.

[1] I. Tanihata, H. Hamagaki, O. Hashimoto, Y. Shida, N. Yoshikawa, K. Sugimoto, O. Yamakawa, T. Kobayashi, and N. Takahashi, Phys. Rev. Lett. **55**, 2676 (1985).
[2] J. Meng, I. Tanihata, and S. Yamaji, Phys. Lett. B **419**, 1 (1998).
[3] J. Meng, S.-G. Zhou, and I. Tanihata, Phys. Lett. B **532**, 209 (2002).
[4] M. Hemalatha, A. Bhagwat, A. Shrivastava, S. Kailas, and Y. K. Gambhir, Phys. Rev. C **70**, 044320 (2004).
[5] M. Hemalatha, N. Maladkar, and S. Kailas, Phys. Rev. C **92**, 024611 (2015).
[6] P. Campbell, I. Moore, and M. Pearson, Prog. Part. Nucl. Phys. **86**, 127 (2016).
[7] K. Blaum, J. Dilling, and W. Nörtershäuser, Phys. Scr. **T152**, 014017 (2013).
[8] H. J. Kluge and Nörtershäuser, Hyperfine Interact. **196**, 295 (2010).
[9] B. Cheal and K. Flanagan, J. Phys. G: Nucl. Part. Phys. **37**, 113101 (2010).
[10] I. Angeli and K. P. Marinova, At. Data Nucl. Data Tables **99**, 69 (2013).
[11] K. Blaum, W. Geithner, J. Lassen, P. Lievens, K. Marinova, and R. Neugart, Nucl. Phys. A **799**, 30 (2008).
[12] Á. Koszorús, X. F. Yang, W. G. Jiang, S. J. Novario, S. W. Bai, J. Billowes *et al.*, Nat. Phys. **17**, 439 (2021).
[13] Á. Koszorús, X. F. Yang, J. Billowes, C. L. Binnersley, M. L. Bissell, T. E. Cocolios *et al.*, Phys. Rev. C **100**, 034304 (2019).
[14] K. Kreim *et al.*, Phys. Lett. B **731**, 97 (2014).
[15] R. F. Garcia Ruiz *et al.*, Nat. Phys. **12**, 594 (2016).
[16] A. J. Miller *et al.*, Nat. Phys. **15**, 432 (2019).
[17] M. Avgoulea *et al.*, J. Phys. G: Nucl. Part. Phys. **38**, 025104 (2011).
[18] Yu. P. Gangrsky and K. P. Marinova, J. Phys. G: Nucl. Part. Phys. **30**, 1089 (2004).
[19] H. Heylen, C. Babcock, R. Beerwerth, J. Billowes, M. L. Bissell, K. Blaum *et al.*, Phys. Rev. C **94**, 054321 (2016).
[20] F. C. Charlwood *et al.*, Phys. Lett. B **690**, 346 (2010).
[21] K. Minamisono, D. M. Rossi, R. Beerwerth, S. Fritzsche, D. Garand, A. Klose *et al.*, Phys. Rev. Lett. **117**, 252501 (2016).
[22] U. C. Perera, A. V. Afanasjev, and P. Ring, Phys. Rev. C **104**, 064313 (2021).
[23] G. A. Lalazissis, A. R. Farhan, and M. M. Sharma, Nucl. Phys. A **628**, 221 (1998).
[24] E. Caurier, K. Langanke, G. Martónez-Pinedo, F. Nowacki, and P. Vogel, Phys. Lett. B **522**, 240 (2001).
[25] K. Zhang *et al.*, At. Data Nucl. Data Tables **144**, 101488 (2022).
[26] T. Nikšić, N. Paar, D. Vretenar, and P. Ring, Comput. Phys. Commun. **185**, 1808 (2014).
[27] G. A. Lalazissis, T. Nikšić, D. Vretenar, and P. Ring, Phys. Rev. C **71**, 024312 (2005).
[28] J. Decharge and D. Gogny, Phys. Rev. C **21**, 1568 (1980).
[29] S. Hilaire and M. Girod, Eur. Phys. J. A **33**, 237 (2007).

[30] J.-P. Delaroche, M. Girod, J. Libert, H. Goutte, S. Hilaire, S. Péru, N. Pillet, and G. F. Bertsch, Phys. Rev. C **81**, 014303 (2010).
[31] J. P. Jeukenne, A. Lejeune, and C. Mahaux, Phys. Rev. C **16**, 80 (1977).
[32] E. Bauge, J. P. Delaroche, and M. Girod, Phys. Rev. C **63**, 024607 (2001).
[33] D. Vautherin, Phys. Rev. C **7**, 296 (1973).
[34] M. Bender, P.-H. Heenen, and P.-G. Reinhard, Rev. Mod. Phys. **75**, 121 (2003).
[35] Y. K. Gambhir, P. Ring, and A. Thimet, Ann. Phys. (NY) **198**, 132 (1990).
[36] D. Vretenar, A. V. Afanasjev, G. A. Lalazissis, and P. Ring, Phys. Rep. **409**, 101 (2005).
[37] T. Nikšić, D. Vretenar, and P. Ring, Prog. Part. Nucl. Phys. **66**, 519 (2011).
[38] J. Meng, H. Toki, S. G. Zhou, S. Q. Zhang, W. H. Long, and L. S. Geng, Prog. Part. Nucl. Phys. **57**, 470 (2006).
[39] S. Shen, H. Liang, W. H. Long, J. Meng, and P. Ring, Prog. Part. Nucl. Phys. **109**, 103713 (2019).
[40] H. Liang, J. Meng, and S.-G. Zhou, Phys. Rep. **570**, 1 (2015).
[41] J. Meng, J. Peng, S. Q. Zhang, and P. W. Zhao, Front. Phys. **8**, 55 (2013).
[42] M. Hemalatha, N. Maladkar, and S. Kailas, EPJ Web Conf. **107**, 08006 (2016).
[43] S. E. Agbemava, A. V. Afanasjev, D. Ray, and P. Ring, Phys. Rev. C **89**, 054320 (2014).
[44] H. Abusara and S. Ahmad, Phys. Rev. C **96**, 064303 (2017).
[45] N. Paar, D. Vretenar, E. Khan, and G. Coló, Rep. Prog. Phys. **70**, 670 (2007).
[46] M. Kleban, B. Nerlo-Pomorska, J. F. Berger, J. Dechargé, M. Girod, and S. Hilaire, Phys. Rev. C **65**, 024309 (2002).
[47] J. Meng and P. Ring, Phys. Rev. Lett. **77**, 3963 (1996).
[48] J. Meng, Nucl. Phys. A **635**, 3 (1998).
[49] S.-G. Zhou, J. Meng, P. Ring, and E.-G. Zhao, Phys. Rev. C **82**, 011301(R) (2010).
[50] L. L. Li, J. Meng, P. Ring, E.-G. Zhao, and S.-G. Zhou, Phys. Rev. C **85**, 024312 (2012).
[51] P. W. Zhao, Z. P. Li, J. M. Yao, and J. Meng, Phys. Rev. C **82**, 054319 (2010).
[52] K. Zhang, M. K. Cheoun, Y. B. Choi, P. S. Chong, J. Dong, L. Geng *et al.*, Phys. Rev. C **102**, 024314 (2020).
[53] K. Zhang, X. He, J. Meng, C. Pan, C. Shen, C. Wang, and S. Zhang, Phys. Rev. C **104**, L021301 (2021).
[54] Y. Tian, Z. Ma, and P. Ring, Phys. Lett. B **676**, 44 (2009).
[55] P. Möller and J. R. Nix, Nucl. Phys. A **536**, 20 (1992).
[56] J.-F. Berger, M. Girod, and D. Gogny, Comput. Phys. Commun. **63**, 365 (1991).
[57] F. Chappert, M. Girod, and S. Hilaire, Phys. Lett. B **668**, 420 (2008).
[58] J. Libert, M. Girod, and J.-P. Delaroche, Phys. Rev. C **60**, 054301 (1999).
[59] CEA database, http://www-phynu.cea.fr/HFB-5DCH-table, and Supplemental Material at http://link.aps.org/supplemental/10.1103/PhysRevC.81.014303.
[60] W. Meng, G. Audi, F. G. Kondev, W. J. Huang, S. Naimi, and X. Xing, Chin. Phys. C **41**, 030003 (2017).
[61] X. W. Xia *et al.*, At. Data Nucl. Data Tables **121-122**, 1 (2018).
[62] I. Angeli and K. P. Marinova, J. Phys. G: Nucl. Part. Phys. **42**, 055108 (2015).
[63] N. Maladkar, M. Hemalatha, and S. Kewat, in *Proceedings of the 64th BRNS DAE Symposium on Nuclear Physics, Lucknow, 2018*, edited by Yogesh K. Gupta, P. C. Rout, L. M. Pant, and B. K. Nayak (Board of Research in Nuclear Sciences, Lucknow, 2019), p. 567.
[64] M. Hemalatha, N. Maladkar, and S. Kailas, Proceedings of the 26th International Nuclear Physics Conference, Adelaide, Australia, 2016 (unpublished).
[65] W. D. Myers and K.-H. Schmidt, Nucl. Phys. A **410**, 61 (1983).
[66] P. Sarriguren, M. K. Gaidarov, E. M. de Guerra, and A. N. Antonov, Phys. Rev. C **76**, 044322 (2007).
[67] M. Arnould and S. Goriely, Nucl. Phys. A **777**, 157 (2006).
[68] M. Arnould, S. Goriely, and K. Takahashi, Phys. Rep. **450**, 97 (2007).
[69] M. Hemalatha, Y. K. Gambhir, W. Haider, and S. Kailas, Phys. Rev. C **79**, 057602 (2009).
[70] D. Pachouri, Syed Rafi, and W. Haider, J. Phys. G: Nucl. Part. Phys. **39**, 055101 (2012).
[71] M. Hemalatha, Y. K. Gambhir, S. Kailas, and W. Haider, Phys. Rev. C **75**, 037602 (2007).
[72] E. Bauge, J. P. Delaroche, and M. Girod, Phys. Rev. C **58**, 1118 (1998).
[73] E. Bauge, J. P. Delaroche, and M. Girod, Nucl. Phys. A **654**, 829c (1999).
[74] E. Khan *et al.*, Nucl. Phys. A **694**, 103 (2001).
[75] W. H. Dickhoff and R. J. Charity, Prog. Part. Nucl. Phys. **105**, 252 (2019).
[76] K. Amos, P. J. Dortmans, H. V. von Geramb, S. Karataglides, and J. Raynal, in *Advances in Nuclear Physics*, edited by J. W. Negele and E. Vogt (Plenum, New York, 2000), Vol. 25, p. 275.
[77] A. J. Koning and J. P. Delaroche, Nucl. Phys. A **713**, 231 (2003).
[78] R. R. Scheerbaum, Nucl. Phys. A **257**, 77 (1976).
[79] N. Aoi, E. Takeshita, H. Suzuki, S. Takeuchi, S. Ota, H. Baba *et al.*, Phys. Rev. Lett. **102**, 012502 (2009).
[80] T. Baugher, A. Gade, R. V. F. Janssens, S. M. Lenzi, D. Bazin, B. A. Brown *et al.*, Phys. Rev. C **86**, 011305(R) (2012).
[81] L. F. Canto, P. R. S. Gomes, R. Donangelo, J. Lubian, and M. S. Hussein, Phys. Rep. **596**, 1 (2015).
[82] J. Raynal, Centre d'Etudes Nucléaires de Saclay Report No. CEA-N-2772, 1994 (unpublished).
[83] T. Noro, H. Sakaguchi, M. Nakamura, K. Hatanaka, F. Ohtani, H. Sakamoto, and S. Kobayashi, Nucl. Phys. A **366**, 189 (1981).
[84] S. Kox, A. Gamp, C. Perrin, J. Arvieux, R. Bertholet, J. F. Bruandet *et al.*, Phys. Rev. C **35**, 1678 (1987).
[85] L. Sihver, M. Lantz, and A. Kohama, Phys. Rev. C **89**, 067602 (2014).
[86] J. J. H. Menet, E. E. Gross, J. J. Malanify, and A. Zucker, Phys. Rev. C **4**, 1114 (1971).
[87] R. F. Carlson, At. Data Nucl. Data Tables **63**, 93 (1996).